
FORECASTING THE AMBIENT SOLAR WIND WITH NUMERICAL MODELS: I. ON THE IMPLEMENTATION OF AN OPERATIONAL FRAMEWORK

A PREPRINT

Martin A. Reiss

Heliophysics Science Division
NASA Goddard
Greenbelt, MD 20771, USA
martin.reiss@nasa.gov

Peter J. MacNeice

Heliophysics Science Division
NASA Goddard
Greenbelt, MD 20771, USA

Leila M. Mays

Heliophysics Science Division
NASA Goddard
Greenbelt, MD 20771, USA

Charles N. Arge

Heliophysics Science Division
NASA Goddard
Greenbelt, MD 20771, USA

Christian Möstl

Space Research Institute
Austrian Academy of Sciences
8042 Graz, Austria

Ljubomir Nikolic

Canadian Hazards Information Service
Natural Resources Canada
Ottawa, Canada

Tanja Amerstorfer

Space Research Institute
Austrian Academy of Sciences
8042 Graz, Austria

2018 December 12

ABSTRACT

The ambient solar wind conditions in interplanetary space and in the near-Earth environment are determined by activity on the Sun. Steady solar wind streams modulate the propagation behavior of interplanetary coronal mass ejections and are themselves an important driver of recurrent geomagnetic storm activity. The knowledge of the ambient solar wind flows and fields is thus an essential component of successful space weather forecasting. Here, we present an implementation of an operational framework for operating, validating, and optimizing models of the ambient solar wind flow on the example of Carrington Rotation 2077. We reconstruct the global topology of the coronal magnetic field using the potential field source surface model (PFSS) and the Schatten current sheet model (SCS), and discuss three empirical relationships for specifying the solar wind conditions near the Sun, namely the Wang-Sheeley (WS) model, the distance from the coronal hole boundary (DCHB) model, and the Wang-Sheeley-Arge (WSA) model. By adding uncertainty in the latitude about the sub-Earth point, we select an ensemble of initial conditions and map the solutions to Earth by the Heliospheric Upwind eXtrapolation (HUX) model. We assess the forecasting performance from a continuous variable validation and find that the WSA model most accurately predicts the solar wind speed time series (RMSE \approx 83 km/s). We note that the process of ensemble forecasting slightly improves the forecasting performance of all solar wind models investigated. We conclude that the implemented framework is well suited for studying the relationship between coronal magnetic fields and the properties of the ambient solar wind flow in the near-Earth environment.

Keywords Solar wind · Solar-terrestrial relations · Sun: heliosphere · Sun: magnetic fields

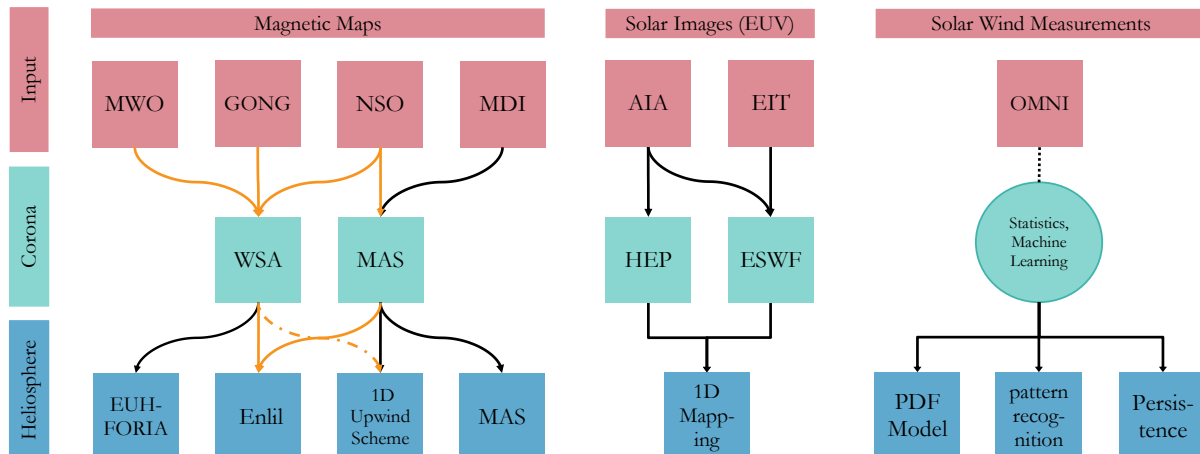


Figure 1: Overview of coronal and heliospheric model combinations for forecasting the ambient solar wind conditions in the near-Earth environment. The orange colored lines highlight models hosted at NASA’s Community Coordinated Modeling Center online platform (see, <https://ccmc.gsfc.nasa.gov/models/>).

1 Introduction

The knowledge of the evolving ambient solar wind is an essential component of successful space weather forecasting [26]. The ambient solar wind flows and fields play an important role in understanding the propagation of coronal mass ejections (CMEs) and are themselves an important driver of recurrent geomagnetic activity. More specifically, high-speed solar wind streams contribute about 70 % of geomagnetic activity outside of solar maximum and about 30 % at solar maximum [34]. Even when the occurrence rate of CMEs increases from 0.3 per day during solar minimum to about 4–5 per day during solar maximum [50], key properties in interplanetary space, such as the solar wind bulk speed, magnetic field strength, and orientation, are determined by the ambient solar wind flow [17].

The topology of open magnetic field lines along which ambient solar wind flows accelerate to supersonic speeds plays a fundamental role in understanding phenomena that drive our evolving space weather. To date, there are no routine measurements of the coronal magnetic field. Magnetic models for the solar corona, therefore, have to rely on extrapolations calculated from the observed line-of-sight component of the photospheric field. The most widely applied extrapolation technique to reconstruct global solutions for the coronal magnetic field is the Potential Field Source Surface model [PFSS; 1, 47]. Using the current-free (or potential field) assumption for regions above the photosphere, solutions for the magnetic field can be expressed as the gradient of a magnetic scalar potential. Since potential fields give closed magnetic fields, a spherical source surface, where the magnetic field is assumed to be only radial is added as an outer boundary condition. The radius of the spherical source surface is an adjustable parameter typically set to a reference height of $2.5 R_0$ to best match observations [8]. To account for *Ulysses* measurements showing latitudinal invariance of the radial magnetic field component [55], the so-called Schatten current sheet (SCS) model [46] is typically added beyond the PFSS model to create a more uniform radial field strength solution.

The effect of the solar wind is to drag and distort magnetic field lines, and thus to distort the coronal field from the assumed current-free configuration. Ideally, a model should account for the complex dynamics of the solar wind flow by solving a set of nonlinear partial differential equations of magnetohydrodynamics (MHD) [e.g., 1]. As such, the Magnetohydrodynamics Algorithm outside a Sphere model [MAS; 16, 21] and the Space Weather Modeling Framework [SWMF; 52] are three-dimensional MHD models. The PFSS solutions are usually used as an initial condition, and the MHD equations are integrated in time until the plasma and magnetic fields relax into equilibrium. The final steady-state solution is characterized by closed magnetic fields that confine the solar wind plasma and open magnetic field lines along which solar wind flows accelerate to supersonic speeds.

The state-of-the-art framework for forecasting the ambient solar wind couples models of the corona with those of the inner heliosphere [37, 13]. The coronal part spans the range from 1 solar radii (R_0) to $2.5 R_0$ (PFSS), or $20 R_0$ to $30 R_0$ (MHD). The inner boundary condition of the heliospheric part either results directly from the coronal model or is computed from the topology of the coronal magnetic field. The outer boundary condition computed from the coronal model is used as inner boundary condition for the heliospheric model ($20\text{--}30 R_0$ to 1 au). Typically, the

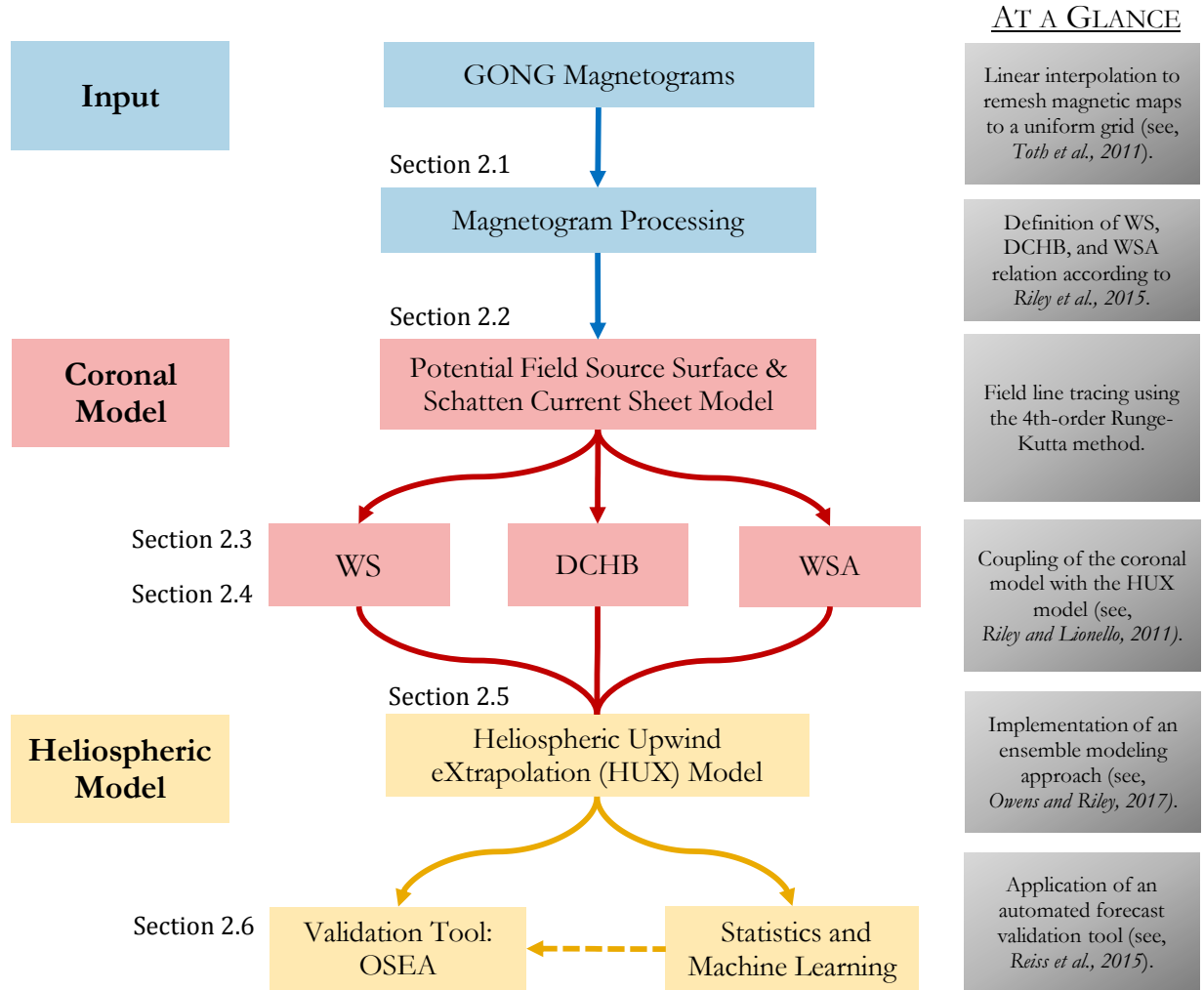


Figure 2: Breakdown structure of the framework implementation. The sections explaining the corresponding framework component are indicated.

heliospheric model is based on the MAS model [16, 21], Enlil [25], or the recently developed European Heliospheric Forecasting Information Asset [EUHFORIA; 32], each of which are three-dimensional numerical MHD models that derive stationary solutions for the ambient solar wind in interplanetary space. Figure 1 shows some different coronal and heliospheric model combinations, together with other approaches for forecasting the ambient solar wind based on empirical relationships [e.g., 43, 53, 49, 33], and statistics or machine learning techniques [e.g., 29, 42]. The orange colored lines highlight models accessible online at NASA’s Community Coordinated Modeling Center (CCMC) online platform.

Many recent studies [e.g., 28, 9, 6, 33] have assessed the performance of operational frameworks for forecasting the ambient solar wind and reported typical uncertainties of about 1 day in the arrival time of high-speed streams. Furthermore, it is now well established that the performance of models of the ambient solar wind is, if at all, only slightly better than a 27 day persistence model [e.g., 29, 12], assuming that the near-Earth solar wind conditions will replicate after each Carrington Rotation (CR). Overall, these results highlight the fact that forecasting the conditions in the ambient solar wind in interplanetary space and in the near-Earth environment is challenging, even during times of low solar activity when the large-scale interplanetary magnetic field configuration evolves less rapidly and disturbances due to CMEs are less frequent [26]. As outlined in the space weather roadmap for the years 2015–2025 [see, 48], continued efforts are needed to improve our capabilities for forecasting the conditions in the ambient solar wind.

In this paper, we present an implementation of a numerical framework for operating, validating, and optimizing models of the evolving ambient solar wind. To study a large number of initial conditions, we rely on the coupling between well-

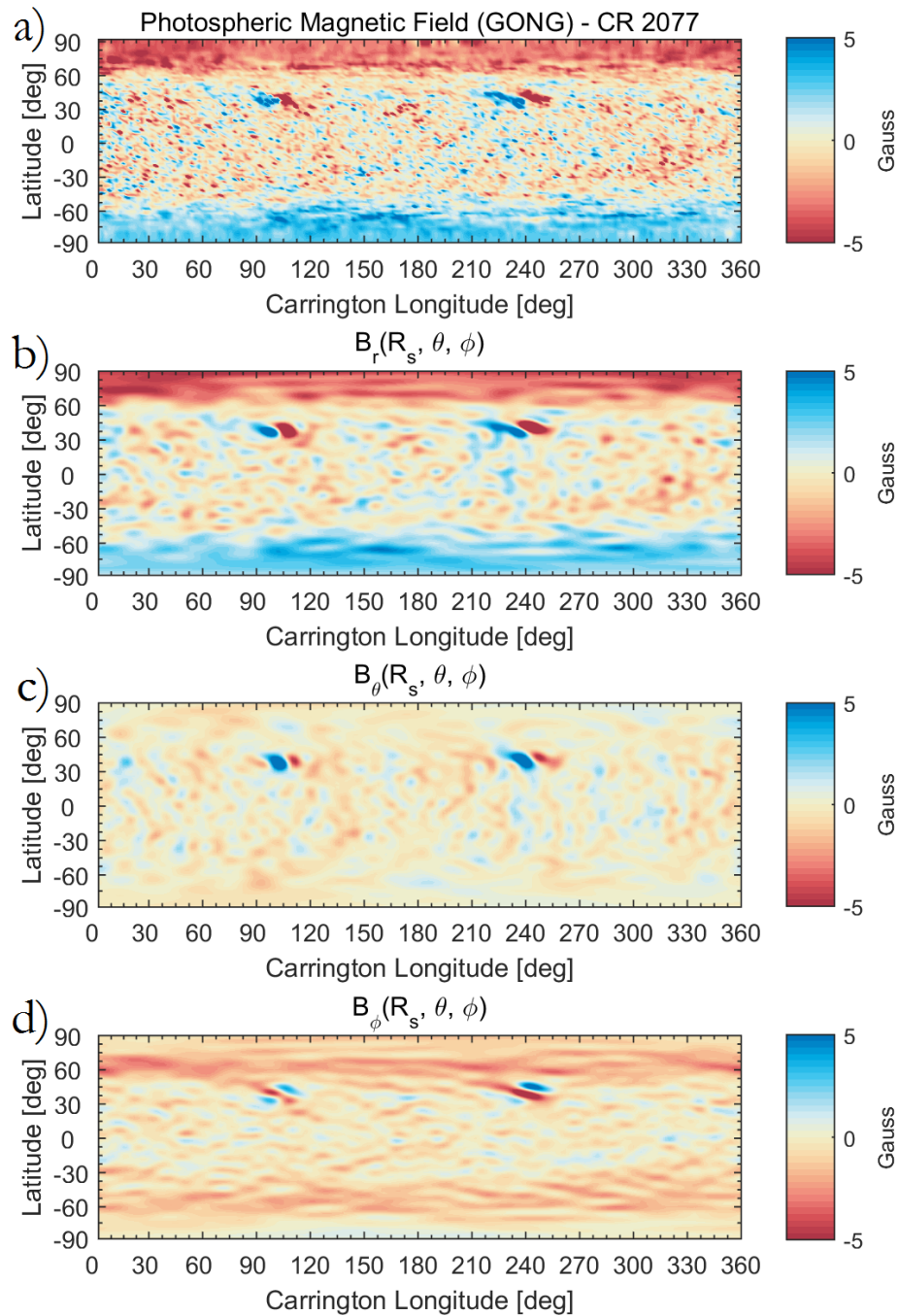


Figure 3: Comparison of the observed line-of-sight component of the photospheric field and the PFSS model solution as a function of the heliographic latitude and Carrington longitude for CR2077 (i.e., 2008 November 20–December 17). The magnetic field strength is saturated at ± 5 G. (a) Remeshed GONG synoptic magnetogram with $N_\theta = 181$; (b)–(d) Magnetic field solutions B_r , B_θ , and B_ϕ computed from the PFSS model using the spherical harmonics expansion up to the order of 80 spherical harmonics.

established coronal models [54, 37, 5] and the Heliospheric Upwind eXtrapolation (HUX) model [35] that bridges the gap of ballistic mapping and MHD modeling. While this paper outlines the breakdown structure and the mathematical foundation of the operational framework, a subsequent paper will be devoted to the validation and optimization of the numerical models by examining the relationship between the coronal magnetic fields and properties of the ambient solar wind. This paper is organized into three sections. In Section 2, we discuss the numerical framework for forecasting the ambient solar wind, including the remeshing of magnetograms (Section 2.1), the magnetic model of the solar corona (Section 2.2), the features of the coronal field solution (Section 2.3), the empirical relationships for specifying the solar wind conditions near the Sun (Section 2.4), the mapping of the solar wind solutions to Earth (Section 2.5), the application of a sensitivity analysis (Section 2.6), and the quantification of the forecasting performance (Section 2.7); and in Section 3 we conclude with a summary of the results and outline future applications of the framework.

2 Description of the Numerical Framework

We present an implementation of a numerical framework for operating, validating, and optimizing models of the ambient solar wind. Figure 2 illustrates the breakdown structure of the current framework implementation. The coronal domain spans the range from $1 R_0$ to $5 R_0$, where the outer boundary condition computed from the coronal part is used as an inner boundary condition for the heliospheric domain. The model in the heliospheric domain where the solar wind flow is supersonic then uses the boundary condition as an input for propagating the solar wind solutions near the Sun to 1 au. The subsequent sections are concerned with explaining the components of the framework in detail.

2.1 Input to the Models

We use full-disk photospheric magnetograms from the Global Oscillation Network Group (GONG) from the National Solar Observatory (NSO) as an inner boundary condition for the coronal model. The global maps of the solar magnetic field measured in Gauss (G) are given on the $(\sin \theta, \phi)$ grid with 180×360 grid points, where $\theta \in [0, \pi]$ and $\phi \in [0, 2\pi]$ are the latitude and longitude coordinates, respectively. They are available as near-real-time magnetic maps or full CR maps at the GONG online platform¹. Throughout this paper, we illustrate our model solutions on the example of CR2077 (2008 November 20–December 17), that is, during solar minimum when the global magnetic field is dominated by its dipolar component and pronounced polar coronal holes are observable.

We use the full-disk magnetic maps as an inner boundary condition for the coronal model. The coronal model is based on a spherical harmonic decomposition of the input magnetogram. When the raw magnetogram on the $(\sin \theta, \phi)$ grid is used as an input and the order of spherical harmonics expansion is large compared to the resolution of the magnetic map, inaccurate results, especially at the crucial polar regions, are expected. Tóth et al. [51] concludes that the information from magnetograms is used more efficiently when the input magnetograms (i) are remeshed to a grid that is uniform in the latitude θ , (ii) contain both poles at $\theta = 0$, and $\theta = \pi$, and (iii) have an odd number of grid points.

We remesh the magnetograms according to the linear interpolation procedure discussed in Tóth et al. [51]. To do so, we begin with adding two additional grid cells at the north and south poles of the input magnetic map $M_{i,j}$ with $N_\theta = 180$ and $N_\phi = 360$ grid points in the latitude and longitude, respectively. The values for the extra grid cells at the poles M_0 and $M_{N_\theta+1}$ are given by

$$M_0 = \frac{1}{N_\phi} \sum_{j=1}^{N_\phi} M_{1,j}, \quad (1)$$

and

$$M_{N_\theta+1} = \frac{1}{N_\phi} \sum_{j=1}^{N_\phi} M_{N_\theta,j}. \quad (2)$$

The latitude of the uniform θ grid is

$$\theta'_{i'} = \pi \frac{i' - 1}{N'_\theta - 1}, \quad (3)$$

¹<http://gong.nso.edu>

where N'_θ is the number of grid points at the uniform θ grid, and the index $i' = 1 \dots N'_\theta$. Finally, we interpolate the grid points from the raw magnetogram mesh to the uniform θ mesh using a linear interpolation relation (no magnetic flux conservation) of the form

$$M'_{i',j} = \alpha M_{i,j} + (1 - \alpha)M_{i+1,j}, \quad (4)$$

where the index i is selected so that

$$\theta \leq \theta'_{i'} \leq \theta_{i+1}, \quad (5)$$

and

$$\alpha = \frac{\theta_{i+1} - \theta'_{i'}}{\theta_{i+1} - \theta_i}. \quad (6)$$

Notice that the maximum degree for the expansion of spherical harmonics is now limited only by the anti-alias limit [see, 51] given by

$$\min \left(\frac{2N'_\theta}{3}, \frac{N_\phi}{3} \right). \quad (7)$$

By utilizing remeshed magnetograms as an inner boundary condition for the coronal model, we can, therefore, expect accurate solutions up to the order of 120 spherical harmonics [51]. Figure 3(a) depicts the computed remeshed magnetogram as a function of the heliographic latitude and Carrington longitude for CR2077.

2.2 Magnetic Model of the Solar Corona

The magnetic model of the solar corona couples the PFSS model and the SCS model to reconstruct the coronal magnetic field. The PFSS model is based on the assumptions that the region above the photosphere is current free, and that the magnetic field at an imaginary reference sphere, called the source surface with radius R_1 is radial only [1, 47]. As detailed in Appendix A, Eq.(19) can be solved to derive the magnetic field components at any point in the coronal domain ($R_0 \leq r \leq R_1$). Figure 3 (b)–(d) present the magnetic field components B_r , B_θ , and B_ϕ derived from the PFSS model at the solar surface as a function of the latitude and Carrington longitude for CR2077. We note that we used a color scheme for all illustrations that is color-blind friendly [see, 15]. From the comparison in Figure 3, it is apparent that the PFSS solution using the spherical harmonics expansion up to $n = 80$, is in reasonable agreement with the observed line-of-sight component of the photospheric magnetic field.

To extend the magnetic field solution from the outer boundary of the PFSS model at $2.5 R_0$ to a distance of $R_2 = 5 R_0$, we employ the SCS model [46]. The SCS model uses the PFSS solutions at the source surface as an inner boundary condition. The SCS model is similar to the PFSS model but involves solving an additional Laplace equation with different boundary conditions. In the first step, the magnetic field on the source surface is oriented to point away from the Sun. In other words, the signs of the magnetic field components B_r , B_θ , and B_ϕ are reversed if $B_r < 0$ at the source surface. While the magnetic field solution is defined to vanish at infinity, the non-negative magnetic field values as model input ensure that a thin current sheet is retained in the field solution. The underlying idea of the SCS model is to extend the magnetic field solution in a nearly radial way. To retain the resolution, we match the grid of the SCS model with the PFSS model with equal steps of 2° in latitude and longitude. As discussed in Appendix B, we use estimates of the coefficients g_n^m and h_n^m from the least mean square fit to compute the magnetic field above the source surface. Finally, the polarity needs to be corrected to match the polarities in the region $r \leq R_1$.

The imposed boundary conditions of the PFSS model and the SCS model are not compatible, causing discontinuities in the tangential component of the magnetic field across the source surface. When coupling the PFSS model and SCS model solutions, discontinuities in the form of kinks in the magnetic field topology are observable. In order to account for this effect, [20] proposed a more flexible coupling between the two models. The authors concluded that their approach leads to more accurate forecast results. Following the procedure of [20], we set the radius of the source surface to $2.5 R_0$ but use the PFSS solution at $2.3 R_0$ as an inner boundary condition for the SCS model. By doing so, we couple the PFSS and SCS model solutions and reconstruct the global topology of the coronal magnetic field.

2.3 Computing Features of the Coronal Field Solution

Models for specifying the solar wind conditions near the Sun rely on the areal expansion factor f_p and the great-circle angular distance from the nearest open-closed boundary d , both of which are derived from the coronal magnetic field

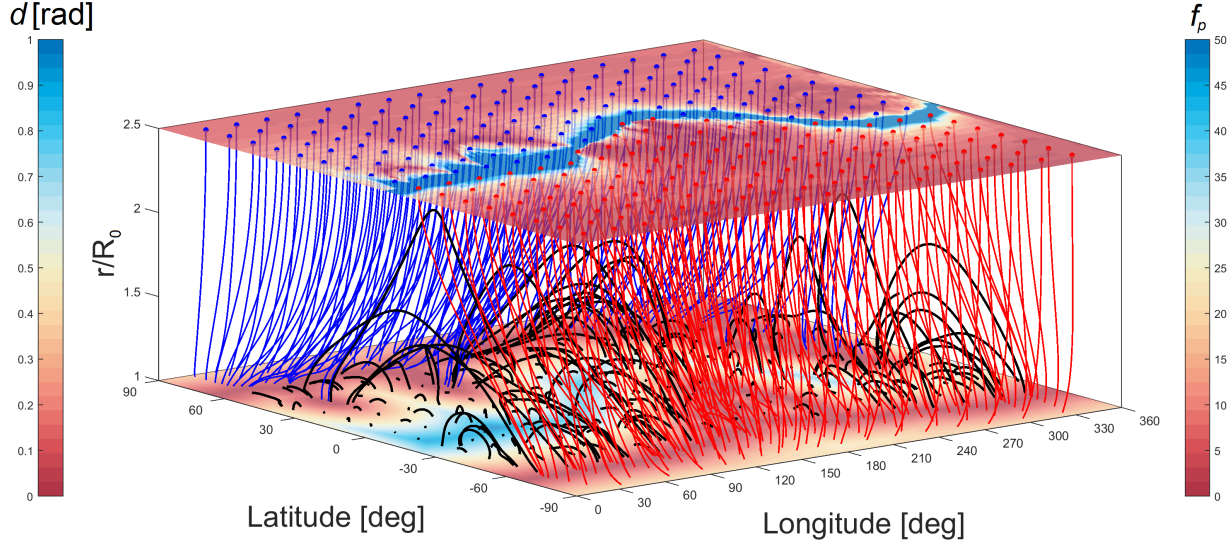


Figure 4: Illustration of the topology of the magnetic field between the photosphere and the source surface at $2.5 R_0$ computed from the described magnetic model of the solar corona for CR2077. Red and blue colors indicate positive and negative magnetic field lines, respectively. While the lower plane shows the great-circle angular distance from the nearest coronal hole boundary at the photosphere d , the upper plane shows the areal expansion factor f_p indicating how much the corresponding flux tube expands between the photosphere and the source surface at $2.5 R_0$.

solution. It is noteworthy that both features are linked to different fundamental theories on the origin of slow solar wind [see, 36, 41]. While the expansion factor assumes that the solar wind flow along open field lines that diverge the most leads to the slow solar wind [54], the distance to the coronal hole boundary is more related to the boundary layer idea of interchange reconnection for the origin of the slow solar wind [3].

To trace magnetic field lines and reconstruct the magnetic field topology in the coronal model domain $R_0 \leq r \leq R_2$, we use a fourth-order Runge-Kutta method (RK4) and solve the following set of equations, expressed as

$$\begin{aligned} \frac{dr}{ds} &= \frac{B_r}{B}, \\ \frac{d\theta}{ds} &= \frac{1}{r} \frac{B_\theta}{B}, \\ \frac{d\phi}{ds} &= \frac{1}{r \sin \theta} \frac{B_\phi}{B}, \end{aligned} \quad (8)$$

where ds is a segment along the magnetic field line.

More specifically, our approach for constructing the large-scale topology of the coronal field is two-fold. First, we start from the base of the model at the solar surface ($r = R_0$) and trace magnetic field lines upwards. When the field line returns to the solar surface, we label the corresponding footpoint at the solar surface as a “closed field”. In contrast, when the field line reaches the upper boundary of the coronal model ($r = R_2$) we label the footpoint as a “open field”. In this way, we compute coronal hole regions, i.e., magnetically open regions expected to guide high-speed solar wind streams out into the heliosphere. Using the location of coronal holes at the solar surface, we run a perimeter tracing algorithm to compute coronal hole boundaries. Then, we compute the great-circle angular distance d between footpoints of open field lines and their nearest coronal hole boundary. Second, we start from the outer boundary of the coronal model ($r = R_2$) and trace the field lines down to the solar surface. By doing so, we compute the areal expansion factor f_p as

$$f_p = \left(\frac{R_0}{R_1} \right)^2 \left| \frac{B_r(R_0, \theta_0, \phi_0)}{B_r(R_1, \theta_1, \phi_1)} \right|, \quad (9)$$

where B_r is the radial magnetic field component at a given reference height. The areal expansion factor is the amount by which a flux tube expands from the solar surface to another reference height in the corona. Figure 4 shows the topology of the coronal magnetic field and illustrates the features d and f_p at the photosphere and the source surface, respectively.

2.4 Computing Solar Wind Speed Maps

The structure in the solar wind flow is governed by the dynamic pressure term in the momentum equation ($\propto \rho v^2$). This indicates that the near-Sun solar wind solution used as an inner boundary condition for heliospheric models is highly sensitive to errors in the computed solar wind bulk speed [41]. Recently, Riley et al. [41] highlighted three empirical relationships for specifying the solar wind speed ($v = v(d, f_p)$) at a reference sphere of $5 R_0$ (or $30 R_0$ for the MAS model). In the literature, these empirical relationships are known as the Wang-Sheeley (WS) model [54], the Distance from the Coronal Hole Boundary (DCHB) model [37], and the Wang-Sheeley-Argé (WSA) model [5].

The WS model is based on the inverse relationship between the solar wind speed and the magnetic field expansion factor [54], namely

$$v_{ws}(f_p) = v_0 + \frac{(v_1 - v_0)}{f_p^\alpha}. \quad (10)$$

Previous research has established that low magnetic field expansion between the photosphere and some reference height in the corona is correlated with a fast solar wind speed [e.g., 14]. For the coefficients in Eq.(10), we use $v_0 = 250$, $v_1 = 660$, and $\alpha = 2/5$ [see, 4].

The DCHB model relates the speed at the photosphere with the distance of an open field footpoint from the coronal hole boundary and maps the calculated solar wind speed solution out along the magnetic field lines to a given reference sphere [37]. The DCHB relation is defined as

$$v_{dchb}(d) = v_0 + \frac{1}{2} (v_1 - v_0) \left[1 + \tanh \left(\frac{d - \epsilon}{w} \right) \right], \quad (11)$$

where ϵ is a measure for the thickness of the slow flow band, and w denotes the width over which the solar wind reaches coronal hole values. For an open field footpoint at the coronal hole boundary, the solar wind speed is equal to v_0 . For a footpoint located deep inside a coronal hole, the solar wind speed is equal to v_1 . Hence, the farther away the footpoint is from a coronal hole boundary, the faster the expected solar wind speed. In this study, we use $v_0 = 350$, $v_1 = 750$, $\epsilon = 0.1$, and $w = 0.05$ [see, 37].

Finally, the WSA model is a hybrid of the WS model and the DCHB model, combining aspects of the expansion factor computed from the topology of the magnetic field and the distance to the coronal hole boundary [5]. The WSA model for specifying solar wind speed is given by

$$v_{wsa}(f_p, d) = v_0 + \frac{(v_1 - v_0)}{(1 + f_p)^\alpha} \left\{ \beta - \gamma \exp \left[-(d/w)^\delta \right] \right\}^3, \quad (12)$$

where α , β , γ , and δ are additional model parameters. For the coefficients in Eq.(12) we use $v_0 = 285$, $v_1 = 910$, $\alpha = 2/9$, $\beta = 1$, $\gamma = 0.8$, $w = 2$, and $\delta = 3$. Figure 5 shows a comparison between the different empirical relationships for specifying a solar wind speed of $v(f_p, d)$ near the Sun.

2.5 Mapping of the Solar Wind to Earth

Numerous models dealing with the mapping of solar wind solutions near the Sun to Earth have been developed. The spectrum extends from a simple ballistic approximation where each parcel of plasma is assumed to travel with a constant speed through the heliosphere to global heliospheric MHD models that aim to cover all relevant dynamical processes [e.g., 38, 25]. In an attempt to bridge the gap, Riley and Lionello [35] developed the Heliospheric Upwind eXtrapolation (HUX) model. Riley and Lionello [35] have simulated the kinematic of the solar wind flow numerically by simplifying the MHD equations as much as possible. By neglecting the pressure gradient and the gravity terms in the fluid momentum equation [e.g., 31] the solar wind solution on a discretized grid may be written as

$$v_{r+1, \phi} = v_{r, \phi} + \frac{\Delta r}{v_{r, \phi}} \frac{\Omega}{\Delta \phi} \left(\frac{v_{r, \phi+1} - v_{r, \phi}}{\Delta \phi} \right), \quad (13)$$

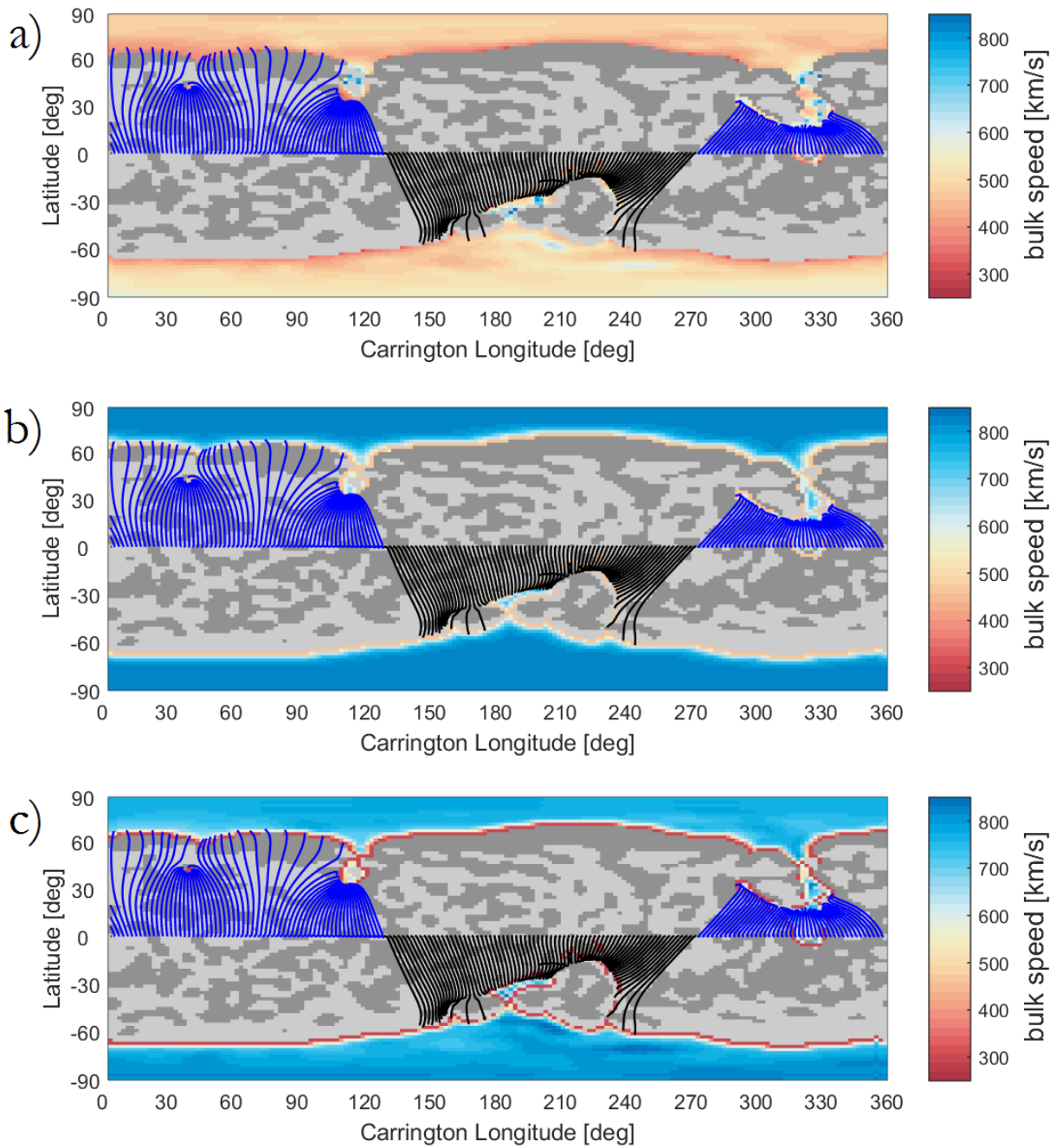


Figure 5: Comparison of empirical relationships for specifying the solar wind speed near the Sun on the example of CR2077. The magnetic field lines illustrate the magnetic connectivity between the computed coronal hole regions and the sub-Earth orbit at the outer boundary of the coronal model ($5 R_0$). The gray colored pixels indicate closed magnetic field topology with negative (dark gray) and positive (light gray) polarity. The full black and blue lines indicate positive and negative magnetic field lines, respectively. (a) Wang-Sheeley (WS) Model; (b) Distance from the Coronal Hole Boundary (DCHB) Model; (c) Wang-Sheeley-Arge (WSA) Model.

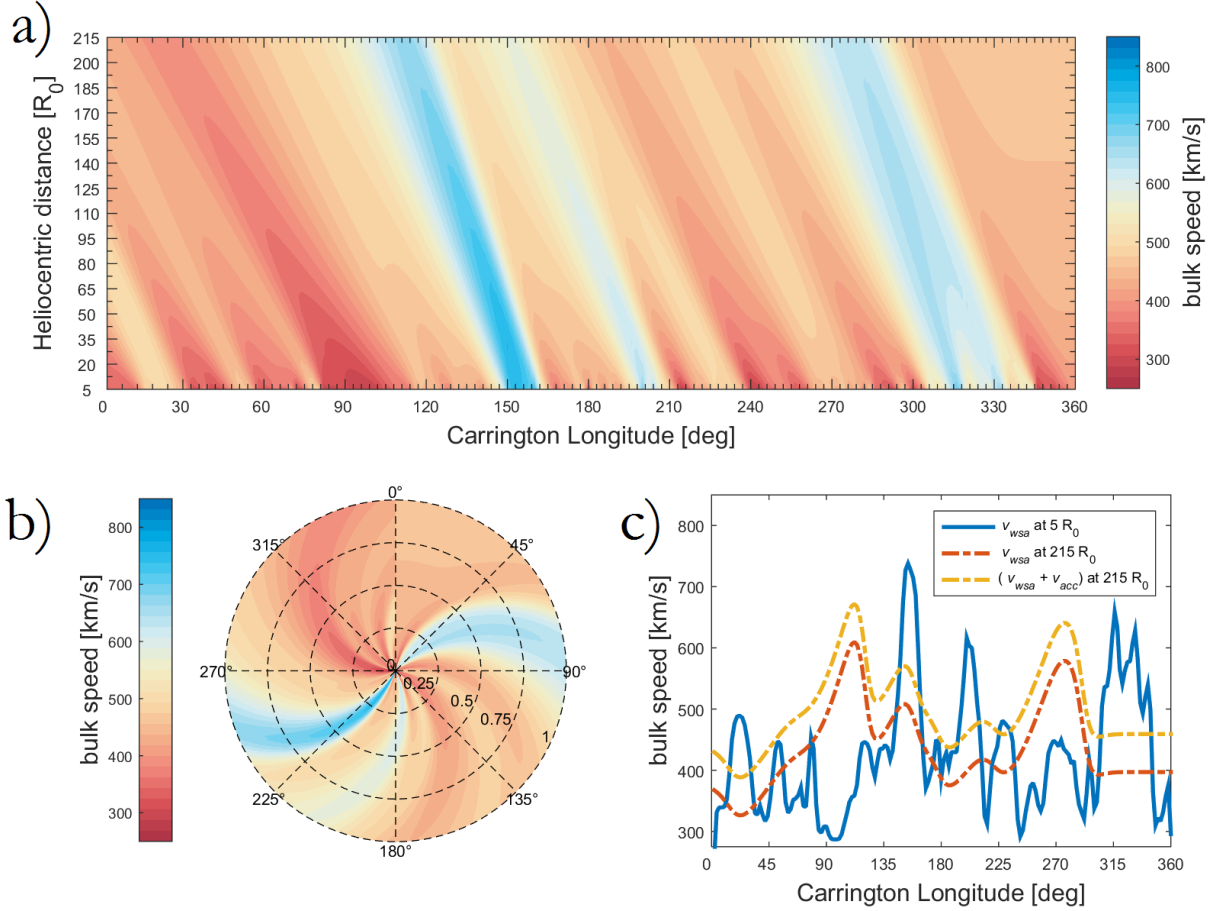


Figure 6: The Heliospheric Upwind eXtrapolation (HUX) model for mapping the WSA solar wind speed solution to 1 au (or $215 R_0$). (a)–(b) Solar wind bulk speed as a function of the heliocentric distance. (c) The input solar wind speed at $5 R_0$ (blue), and the resulting solar wind speed at $215 R_0$ with (yellow) and without (red) the residual speed contribution v_{acc} .

where the subscripts r and ϕ refer to radial and longitudinal grid cells with cell spacings Δr and $\Delta\phi$, and Ω denotes the equatorial angular rotation rate of the Sun (neglecting differential rotation) [see, 35]. In order to match the spatial resolution of the coronal model, we use $\Delta\phi = 2^\circ$ and $\Delta r = 1 R_0$, respectively. As the step size in Δr is increased by two orders of magnitude, the solutions are not significantly different, indicating that the Courant-Friedrichs-Lewy condition for numerical convergence is well met.

Furthermore, Riley and Lionello [35] concluded that it is convenient to account for the residual wind acceleration beyond the coronal model. According to previous model results [e.g., 37, 35], the residual acceleration v_{acc} expected beyond the coronal model is

$$v_{acc}(r) = \alpha v_{r_0} \left[1 - \exp\left(\frac{-r}{r_h}\right) \right], \quad (14)$$

where v_{r_0} is the initial speed at the outer boundary of the coronal model, r is the heliocentric distance, α is a factor by which v_{r_0} is enhanced, and r_h is the scale length for the acceleration (not crucial when mapping the solar wind to 1 au). For the coefficients in Eq.(14) we use $\alpha = 0.15$ and $v_{r_0} = 50 R_0$.

Figure 6 illustrates the HUX model for mapping the solar wind solution near the Sun to Earth. While the top panel shows the propagation of the solar wind solutions in steps of Δr from $5 R_0$ to $215 R_0$ (or 1 au), the bottom panel shows the propagation in spherical coordinates (left) and the calculated speed time series at Earth with and without the residual speed contribution (right). It is also noteworthy that computing the solar wind solution for other heliospheric distances is straightforward. The benefit of the HUX model is that it can match the dynamical evolution explored by global

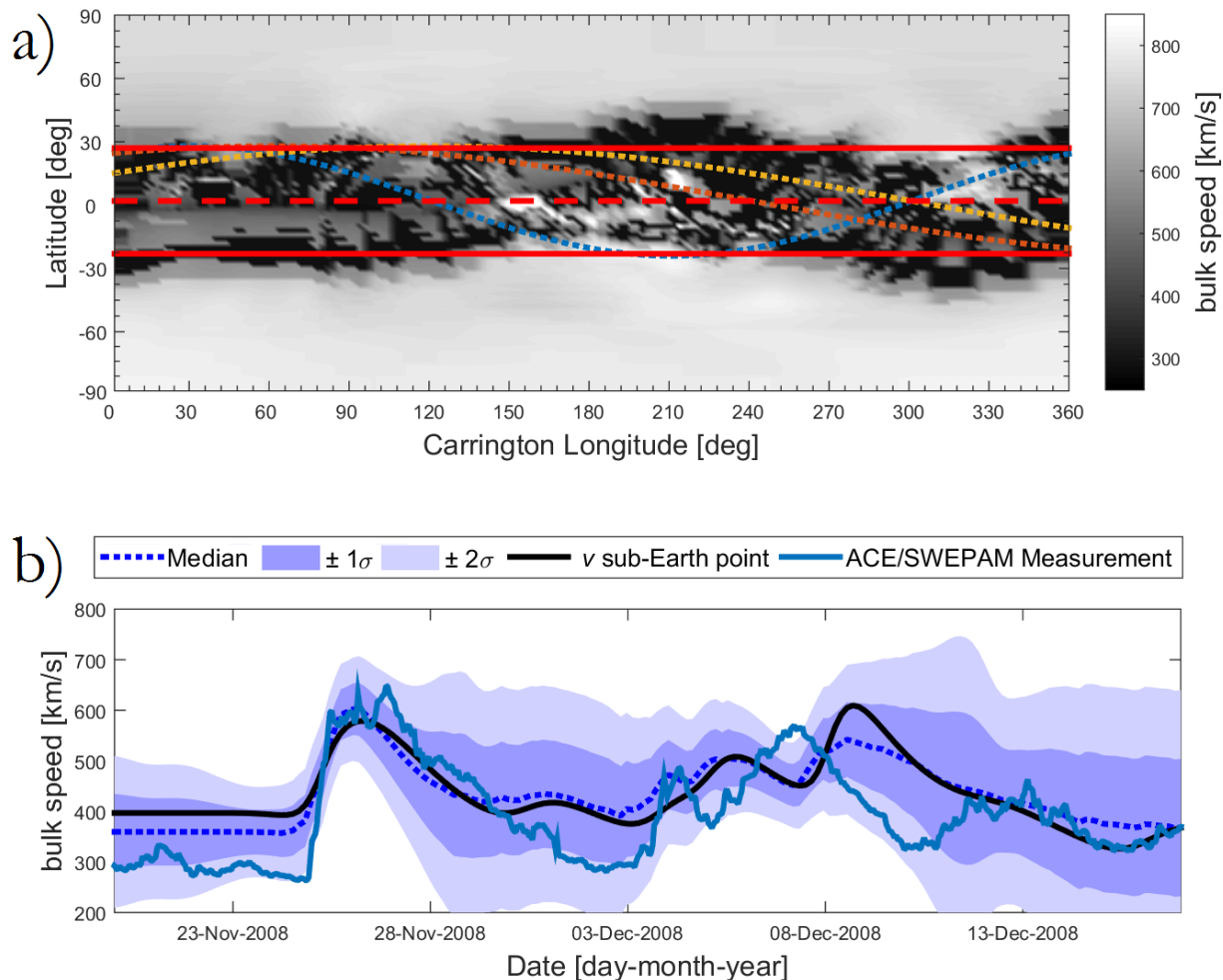


Figure 7: Illustration of the ensemble of initial conditions and the process of mapping the solar wind solutions to Earth by the HUX model. (a) Solar wind solution for CR2077 from the WSA model at $5 R_0$ overlaid with 3 out of 576 individual trajectories together with the median value (dashed red line) and the $\pm 2\sigma$ quantiles (red line); (b) A comparison of observed and WSA model solar wind speed time series at $215 R_0$. The ensemble median of solar wind solutions at Earth is indicated by the dashed blue line and the $\pm 2\sigma$ quantiles are shown in blue color.

heliospheric MHD models that demand only low computational requirements [35]. This is particularly useful to study a large number of initial conditions in the context of ensemble modeling.

2.6 Creating Ensembles of Initial Conditions for Solar Wind Forecasting

The knowledge on the sensitivity of the model performance to initial conditions and model parameter settings is crucial for models of the ambient solar wind. In recent years, the concept of ensemble forecasting has been successfully applied to a number of applications in the space weather forecasting regime. As an example, the sensitivity of PFSS and MHD coronal models on magnetic maps from different observatories has been studied by Riley et al. [39, 40]. More details on recent activities can be found in the reviews by Knipp [11] and Murray [22]. Ensemble forecasting is a technique based on the use of a sample of possible future states to forecast a future state. Intuitively, one would expect that the forecast of the ambient solar wind conditions is very uncertain when the ensemble members (e.g., different solar wind models) are very different from one another. The strength of ensemble forecasting is its capability to deduce confidence bounds by quantifying the uncertainty in the ensemble of possible future states.

Owens et al. [30], for instance, has pointed out that the forecast uncertainty in solar wind models can be studied by adding uncertainty in the sub-Earth orbit at which the coronal solutions near the Sun are sampled. Using the approach

Table 1: The skill of model predictions of solar wind speed for CR2077 in terms of Arithmetic Mean (AM), Standard Deviation (SD), Mean Error (ME), Mean Absolute Error (MAE), and Root-Mean-Square Error (RMSE). A 4-day and 27-day persistence model of near-Earth solar wind conditions provides a baseline against which solar wind models can be compared.

| Model | AM [km/s] | SD [km/s] | ME [km/s] | MAE [km/s] | RMSE [km/s] |
|------------------------|-----------|-----------|-----------|------------|-------------|
| WS | 428.79 | 62.63 | -27.90 | 74.09 | 85.27 |
| DCHB | 379.47 | 30.93 | 21.42 | 83.83 | 103.43 |
| WSA | 437.14 | 69.14 | -36.25 | 68.54 | 82.62 |
| Ensemble Median (WS) | 435.55 | 51.84 | -34.66 | 71.52 | 83.36 |
| Ensemble Median (DCHB) | 367.47 | 4.62 | 33.43 | 78.27 | 100.04 |
| Ensemble Median (WSA) | 437.48 | 63.64 | -36.56 | 62.24 | 74.86 |
| Persistence (4-days) | 394.76 | 99.23 | 6.13 | 130.48 | 161.99 |
| Persistence (27-days) | 409.94 | 108.91 | -9.05 | 66.54 | 78.86 |
| Observation | 400.89 | 96.12 | - | - | - |

of Owens et al. [30], we perform a sensitivity analysis that considers ensemble members at perturbed latitudes θ_p around the sub-Earth orbit given by

$$\theta_p(\phi) = \theta_E + \theta_1 \sin(n\phi + \phi_0), \quad (15)$$

where ϕ is the corresponding Carrington longitude; θ_E is the sub-Earth latitude; θ_1 is the amplitude of the deviation; n is the wave number, indicating how many oscillations the perturbed trajectory completes; and ϕ_0 is the phase offset, indicating how two perturbed trajectories can be out of synchronicity with each other. For the coefficients in Eq.(14), we select $\theta_1 \in [0^\circ, 15^\circ]$ in 1° steps, $n \in [0, 1]$ in 0.5 steps, and $\theta_0 \in [0^\circ, 330^\circ]$ in 30° steps, which ensures that all latitudes are well represented at each longitude [see, 30].

Figure 7(a) shows three individual trajectories together with the median value and the $\pm 2\sigma$ quantiles of the ensemble members. In this way, we obtain information from a sampling of 576 initial speed solutions, each of which are mapped to Earth using the HUX model as outlined in Section 2.5. Figure 7(b) compares the resulting ensemble median at $215 R_0$ and the observed solar wind speed in the near-Earth environment. In this study, the ensemble median is the preferred average measure as the ensembles of solar wind solutions around the sub-Earth latitude are often highly skewed, such that the ensemble mean can yield very biased measures of the ensemble average. Further, we note that ensemble averaging of possible future states is not necessarily expected to provide a systematic improvement of deterministic forecasts [see, 10]. As discussed in Owens et al. [30] and Henley and Pope [7], it is the assessment of forecast uncertainty that is the key advantage of the ensemble approach rather than the ensemble average providing an improved deterministic forecast.

2.7 Assessing the Forecast Performance

The information from the implemented models is used most efficiently when the uncertainty of their results is constantly validated. To enable that, we measure the performance of the framework by the Operational Solar Wind Evaluation Algorithm [OSEA; 33]. OSEA² runs various validation procedures to compare the forecasts and the observations to which they pertain. Traditionally, the relationship between forecast and observation can be studied in terms of continuous variables and binary variables. While the former can take on any real values, the latter is restricted to two possible values such as event/non-event. In the context of solar wind forecasting, the solar wind speed time series can be interpreted in terms of both aspects. The forecasting performance can either be evaluated in terms of an average error or in terms of the capability of forecasting events of an enhanced solar wind speed [27, 18, 19]. OSEA is capable of quantifying both aspects, i.e., a continuous variable evaluation that uses simple point-to-point comparison metrics and an event-based validation analysis that assesses uncertainty of the arrival time of high-speed solar wind streams at Earth.

As an example, Table 1 lists the results obtained from the continuous variable validation of different solar wind models for CR2077 in terms of Arithmetic Mean (AM), Standard Deviation (SD), Mean Error (ME), Mean Absolute Error (MAE), and Root-Mean-Square Error (RMSE). A 4 day and 27 day persistence model of near-Earth solar wind conditions provides a baseline against which the performance can be compared. We find that the RMSE for the WS model, DCHB model, and WSA model is 85.27 km/s, 103.43 km/s, and 82.62 km/s, respectively. The 27 day persistence model has the same statistics as the measurements and greatly benefits from the quasi-steady and recurrent nature of the evolving ambient solar wind in the solar minimum phase and thus is expected to score very high in all measures

²<https://bitbucket.org/reissmar/solar-wind-forecast-verification>

(e.g., $RMSE = 78.86$ km/s). We conclude that the WSA model gives the best forecast results in terms of a continuous variable validation and that the process of ensemble forecasting slightly improves the performance of all solar wind models in this study. It is important to note that the present analysis is indented to illustrate the application of the implemented framework components, which means that our results apply only to CR2077 and that our conclusions are not reliable as a general guide.

3 Discussion

We present a numerical framework for forecasting the evolving ambient solar wind that uses magnetic maps as an input for the PFSS and SCS model to reconstruct the global topology of the coronal magnetic field, specifies the solar wind speed using different established empirical relationships (WS, DCHB, and WSA models) based on the areal expansion factor and the distance to the nearest coronal hole boundary, maps the near-Sun solar wind solution outward to Earth by the HUX model, creates an ensemble of initial conditions by adding uncertainty in the latitude about the sub-Earth point, and uses an automated forecast validation module to quantitatively assess the forecasting skill. The framework relies on established models of the ambient solar wind and is conceptually very similar to already existing numerical frameworks. We carefully compared our model solutions to existing frameworks [e.g., 24, 5], and found that our modular framework implementation in the C++ and Matlab programming language using tools from the Armadillo library [45] is both robust and fast.

The coronal part of the framework relies on empirical relationships between the magnetic field topology and the near-Sun solar wind conditions [54, 37, 5]. Ideally, one would prefer the application of a physics-based MHD model for the corona to capture the complex dynamics at solar wind stream interaction regions, which are not included in the described model approach. Nevertheless, recent studies have shown that the forecast skill of empirical and full physics-based coupled corona-heliosphere models in terms of established metrics is very similar. As an example, [28] studied the performance of different forecast models (WSA, WSA-Enlil, and MAS-Enlil) over an 8 yr period and concluded that the coupled empirical approach currently gives the best forecast results in terms of the mean square error. Considering the trade-off between accuracy and computational requirements of a full MHD code, it thus seems reasonable to follow the described methodology in the context of solar wind forecasting. We conclude that the efficient implementation of the framework using the heliospheric HUX model is well suited for studying the long-term relationship between coronal magnetic fields and the properties of the ambient solar wind.

In the future, we shall work on several topics to try to improve the forecasting performances. While this study presents the implementation of the numerical framework, a subsequent paper will be devoted to the validation and optimization of the present solar wind models. By studying the coupling between magnetic models of the corona and those of the inner heliosphere, we aim toward optimizing the empirical relationships for specifying solar wind properties to advance further their predictive capabilities. In context, a reliable forecast of the ambient solar wind might be beneficial for forecasting the arrival of CMEs. Here, we plan to combine the ambient solar wind framework with the ELlipse Evolution model based on Heliospheric Imager observations [ELEvoHI; 44, 2]. The kinematics of the elliptical-shaped CME front in the ELEvoHI model is governed by the ambient solar wind flow. In the current version of ELEvoHI, the solar wind speed is assumed to be constant during the propagation of the CME in the inner heliosphere. Therefore, we would also like to include information on the complex dynamics of the evolving ambient solar wind to simulate the dynamic deformation of the CME front during the propagation phase. To make the model runs accessible to the space weather community, we also plan to install a later version of the solar wind framework at NASA's CCMC online platform. The release of this online resource is scheduled for 2019 July.

Acknowledgments

The work utilizes data obtained by the Global Oscillation Network Group (GONG) Program, managed by the National Solar Observatory, which is operated by AURA, Inc. under a cooperative agreement with the National Science Foundation. The data were acquired by instruments operated by the Big Bear Solar Observatory, High Altitude Observatory, Learmonth Solar Observatory, Udaipur Solar Observatory, Instituto de Astrofísica de Canarias, and Cerro Tololo Interamerican Observatory. L.N. performed this work as part of Natural Resources Canada's Public Safety Geoscience program. M.A.R., C.M. and T.A. acknowledge the Austrian Science Fund (FWF): J4160-N27, P26174-N27 and P31265-N27.

A PFSS Model

The PFSS model is based on the assumption that the magnetic field \mathbf{B} above the photosphere is current free ($\nabla \times \mathbf{B} = 0$). With this approximation, the magnetic field can be expressed as the gradient of a scalar potential Ψ ,

$$\mathbf{B} = -\nabla\Psi. \quad (16)$$

Using $\nabla \cdot \mathbf{B} = 0$, which expresses the fact that there are no magnetic monopoles, we can write the Laplace equation for the potential Ψ as

$$\nabla^2\Psi = 0. \quad (17)$$

The solution of the Laplace equation in spherical coordinates with $\theta \in [0, \pi]$ and $\phi \in [0, 2\pi]$ in the region $R_0 \leq r \leq R_1$ can be expressed as a infinite series of spherical harmonics expressed as

$$\begin{aligned} \Psi(r, \theta, \phi) = & \left[R_0 \left(\frac{R_0}{r} \right)^{n+1} - R_1 \left(\frac{R_0}{R_1} \right)^{n+2} \left(\frac{r}{R_1} \right)^n \right] \\ & \times \sum_{n=1}^{\infty} \sum_{m=0}^n (g_n^m \cos m\phi + h_n^m \sin m\phi) P_n^m(\cos \theta), \end{aligned} \quad (18)$$

where $R_1 = 2.5 R_0$ is the source surface radius, $P_n^m(\cos \theta)$ are the associated Legendre polynomials, and g_n^m and h_n^m are coefficients that are computed from the input magnetograms. Using Eq.(A1), the solution for the magnetic field components is given by

$$\mathbf{B} = (B_r, B_\theta, B_\phi) = \left(-\frac{\partial\Psi}{\partial r}, -\frac{1}{r} \frac{\partial\Psi}{\partial\phi}, -\frac{1}{r \sin\theta} \frac{\partial\Psi}{\partial\theta} \right). \quad (19)$$

The magnetic field components are computed as follows:

$$\begin{aligned} B_r = & \left[(n+1) \left(\frac{R_0}{r} \right)^{n+2} + \left(\frac{R_0}{R_1} \right)^{n+2} \left(\frac{r}{R_1} \right)^{n-1} \right] \\ & \times \sum_{n=1}^{\infty} \sum_{m=0}^n (g_n^m \cos m\phi + h_n^m \sin m\phi) P_n^m(\cos \theta), \end{aligned} \quad (20)$$

$$\begin{aligned} B_\theta = & - \left[\left(\frac{R_0}{r} \right)^{n+2} - \left(\frac{R_0}{R_1} \right)^{n+2} \left(\frac{r}{R_1} \right)^{n-1} \right] \\ & \times \sum_{n=1}^{\infty} \sum_{m=0}^n (g_n^m \cos m\phi + h_n^m \sin m\phi) P_n^m(\cos \theta), \end{aligned} \quad (21)$$

$$\begin{aligned} B_\phi = & \left[\left(\frac{R_0}{r} \right)^{n+2} - \left(\frac{R_0}{R_1} \right)^{n+2} \left(\frac{r}{R_1} \right)^{n-1} \right] \\ & \times \sum_{n=1}^{\infty} \sum_{m=0}^n \frac{m}{\sin\theta} (g_n^m \sin m\phi - h_n^m \cos m\phi) P_n^m(\cos \theta). \end{aligned} \quad (22)$$

To compute the coefficients g_n^m and h_n^m , we multiply Eq.(A3) for $r = R_0$ with $P_{n'}^{m'} \cos m'\phi$ and $P_{n'}^{m'} \sin m'\phi$, respectively. Using the orthogonality of the Schmidt normalized Legendre polynomials and integrating over the spherical surface, we find

$$\frac{1}{4\pi} \int_0^\pi \int_0^{2\pi} P_n^m(\theta) \begin{Bmatrix} \cos m\phi \\ \sin m\phi \end{Bmatrix} P_{n'}^{m'}(\theta) \begin{Bmatrix} \cos m'\phi \\ \sin m'\phi \end{Bmatrix} \sin\theta d\theta d\phi = \frac{1}{2n+1} \delta_n^{n'} \delta_m^{m'}. \quad (23)$$

This yields the solution of the coefficients g_n^m and h_n^m in the form

$$\begin{Bmatrix} g_n^m \\ h_n^m \end{Bmatrix} = \frac{2n+1}{4\pi \left(n+1 + n \left(\frac{R_0}{R_1} \right)^{2n+1} \right)} \int_0^\pi d\theta \sin \theta P_n^m(\theta) \int_0^{2\pi} d\phi B_r(R_0, \theta, \phi) \begin{Bmatrix} \cos m\phi \\ \sin m\phi \end{Bmatrix}. \quad (24)$$

For the use of remeshed magnetograms as described in Section 2.1, we modify this relation to a discrete representation. To do so, we use the Clenshaw-Curtis quadrature rule given by

$$\int_0^\pi d\theta \sin \theta F(\theta) \approx \sum_{i=1}^{N_\theta} \epsilon_i w_i F(\theta_i), \quad (25)$$

where ϵ_i is $1/2$ for $i = 0$ or $i = H$, and 1 elsewhere. The weights w_i are given by

$$w_i = -\frac{2}{H} \sum_{k=0}^H \frac{\epsilon'_k}{4k^2 - 1} \cos \left(\frac{\pi k(i-1)}{H} \right) \quad (26)$$

where $H = (H_\theta - 1)/2$, ϵ'_k is $1/2$ for $i = 0$ or $i = H$, and 1 elsewhere. Using this equation, we write Eq.(A9) as

$$\begin{Bmatrix} g_n^m \\ h_n^m \end{Bmatrix} = \frac{2n+1}{4\pi \left(n+1 + n \left(\frac{R_0}{R_1} \right)^{2n+1} \right)} \frac{2\pi}{N_\phi} \sum_{i=1}^{N_\theta} \sum_{j=1}^{N_\phi} \epsilon_i w_i P_n^m(\theta_i) B_r(R_0, \theta_i, \phi_j) \begin{Bmatrix} \cos m\phi_j \\ \sin m\phi_j \end{Bmatrix}. \quad (27)$$

Using Eq.(A4) and Eq.(A10), we compute the magnetic field components at any point in the region between the solar surface and the source surface [e.g., 1, 23].

B SCS Model

The solution for the Laplace equation not bounded by the spherical source surface is given by

$$\Psi = R_0 \sum_{n=0}^{\infty} \sum_{m=0}^n \left[\left(\frac{R_0}{r} \right)^{n+1} (g_n^m \cos m\phi + h_n^m \sin m\phi) P_n^m(\phi) \right]. \quad (28)$$

In the SCS model, solutions for the PFSS model for the magnetic field on the source surface are first oriented to point away from the Sun. This means that if $B_r < 0$ on the source surface, the sign of all components B_r , B_θ , and B_ϕ are reversed. In this study, we match the grid of the PFSS model to the SCS model with equal steps of 2° in latitude and longitude. The components of the magnetic field beyond the source surface are

$$\begin{aligned} B_r &= -\frac{d\Psi}{dr} = \sum_{n=1}^{\infty} (n+1) \left(\frac{R_1}{r} \right)^{n+2} \sum_{m=0}^n (g_n^m \cos m\phi + h_n^m \sin m\phi) P_n^m(\cos \theta), \\ B_\theta &= -\frac{1}{r} \frac{d\Psi}{d\theta} = -\sum_{n=1}^{\infty} \left(\frac{R_1}{r} \right)^{n+2} \sum_{m=0}^n (g_n^m \cos m\phi + h_n^m \sin m\phi) \frac{dP_n^m(\cos \theta)}{d\theta}, \\ B_\phi &= -\frac{1}{r \sin \theta} \frac{d\Psi}{d\phi} = \sum_{n=1}^{\infty} \left(\frac{R_1}{r} \right)^{n+2} \sum_{m=0}^n \frac{m}{\sin \theta} (g_n^m \sin m\phi - h_n^m \cos m\phi) P_n^m(\cos \theta). \end{aligned} \quad (29)$$

In this way, we ensure that no closed magnetic field exists beyond the source surface. We use the least-squares approach to best fit the vector field on the source surface. In order to minimize the sum of squared residuals, we write

$$F = \sum_{i=1}^{N_i} \sum_{j=1}^{N_j} \sum_{k=1}^3 \left[B_k(\theta_i, \phi_j) - \sum_{n=0}^{N_s} \sum_{m=0}^n (g_n^m \alpha_{nmk}(\theta_i, \phi_j) + h_n^m \beta_{nmk}(\theta_i, \phi_j)) \right]^2, \quad (30)$$

where $B_k(\theta_i, \phi_j)$ is the reoriented field of the source surface, and the index $k = 1, 2$, and 3 refers to the radial, latitudinal, and azimuthal fields component of the grid point (θ_i, ϕ_j) of the reoriented magnetic field. Further, α_{nmk} and β_{nmk} are

$$\begin{aligned}
 \alpha_{nm1} &= (n+1) \cos m\phi P_n^m(\theta) \\
 \alpha_{nm2} &= -\cos m\phi \frac{dP_n^m(\theta)}{d\theta} \\
 \alpha_{nm3} &= \frac{m}{\sin \theta} \sin m\phi P_n^m(\theta) \\
 \beta_{nm1} &= (n+1) \sin m\phi P_n^m(\theta) \\
 \beta_{nm2} &= -\sin m\phi \frac{dP_n^m(\theta)}{d\theta} \\
 \beta_{nm3} &= \frac{m}{\sin \theta} \cos m\phi P_n^m(\theta)
 \end{aligned} \tag{31}$$

We compute the derivations to minimize F given by $\partial F / \partial g_n^m$, and $\partial F / \partial h_n^m$. For each (n, m) we can write

$$\begin{aligned}
 \sum_i \sum_j \sum_k \alpha_{nmk}(\theta_i, \phi_j) \left(B_k(\theta_i, \phi_j) - \sum_{t=0}^{N_s} \sum_{s=0}^t g_t^s \alpha_{tsk}(\theta_i, \phi_j) + h_t^s \beta_{tsk} \right) &= 0, \\
 \sum_i \sum_j \sum_k \beta_{nmk}(\theta_i, \phi_j) \left(B_k(\theta_i, \phi_j) - \sum_{t=0}^{N_s} \sum_{s=0}^t g_t^s \alpha_{tsk}(\theta_i, \phi_j) + h_t^s \beta_{tsk} \right) &= 0.
 \end{aligned} \tag{32}$$

The same expression in matrix form is

$$\widehat{\alpha\beta} \cdot \widehat{B} = \widehat{\alpha\beta} \cdot \widehat{\alpha\beta}^\top \cdot \widehat{GH}, \tag{33}$$

with

$$\widehat{B} = \begin{bmatrix} B_1(\theta_1, \phi_1) \\ B_1(\theta_1, \phi_2) \\ \vdots \\ B_1(\theta_I, \phi_J) \\ B_2(\theta_1, \phi_1) \\ \vdots \\ B_3(\theta_I, \phi_J) \end{bmatrix}, \quad \widehat{GH} = \begin{bmatrix} g_0^0 \\ g_1^0 \\ \vdots \\ g_N^N \\ h_1^1 \\ \vdots \\ h_N^N \end{bmatrix}, \quad \widehat{\alpha\beta} = \begin{bmatrix} \alpha_{001} & \dots & \alpha_{003} \\ \vdots & & \vdots \\ \alpha_{N_s N_s 1} & \dots & \alpha_{N_s N_s 3} \\ \beta_{111} & \dots & \beta_{003} \\ \vdots & & \vdots \\ \beta_{N_s N_s 1} & \dots & \beta_{N_s N_s 3} \end{bmatrix}. \tag{34}$$

Here, the dimension of \widehat{B} is $3IJ \times 1$, the dimension of \widehat{GH} is $(N_s+1)^2 \times 1$, and the dimension of $\widehat{\alpha\beta}$ is $(N_s+1)^2 \times 3IJ$. By choosing $\widehat{AB} = \widehat{\alpha\beta} \cdot \widehat{\alpha\beta}^\top$ we find that the solution for GH is of the form

$$GH = AB^{-1} \cdot \alpha\beta \cdot B \tag{35}$$

This means that the solution of GH requires the inversion of the square matrix \widehat{AB} . Finally, we use the estimates of g_n^m and h_n^m from the least mean square fit to compute the magnetic field solution above the source surface. We note that the polarity needs to be refined to match the polarities for $r \leq R_1$.

References

- [1] M. D. Altschuler and G. Newkirk. Magnetic Fields and the Structure of the Solar Corona. I: Methods of Calculating Coronal Fields. *Solar Phys.*, 9:131–149, September 1969.
- [2] T. Amerstorfer, C. Möstl, P. Hess, M. Temmer, M. L. Mays, M. Reiss, P. Lowrance, and P.-A. Bourdin. Ensemble Prediction of a Halo Coronal Mass Ejection Using Heliospheric Imagers. *Space Weather*, 16:784–801, July 2018.
- [3] S. K. Antiochos, Z. Mikić, V. S. Titov, R. Lionello, and J. A. Linker. A Model for the Sources of the Slow Solar Wind. *Astrophys. J.*, 731:112, April 2011.
- [4] C. N. Arge and V. J. Pizzo. Improvement in the prediction of solar wind conditions using near-real time solar magnetic field updates. *J. Geophys. Res.*, 105:10465–10480, May 2000.
- [5] C. N. Arge, D. Odstrcil, V. J. Pizzo, and L. R. Mayer. Improved Method for Specifying Solar Wind Speed Near the Sun. In M. Velli, R. Bruno, F. Malara, and B. Bucci, editors, *Solar Wind Ten*, volume 679 of *American Institute of Physics Conference Series*, pages 190–193, September 2003.
- [6] A. Devos, C. Verbeeck, and E. Robbrecht. Verification of space weather forecasting at the Regional Warning Center in Belgium. *Journal of Space Weather and Space Climate*, 4(27):A29, October 2014.
- [7] E. M. Henley and E. C. D. Pope. Cost-Loss Analysis of Ensemble Solar Wind Forecasting: Space Weather Use of Terrestrial Weather Tools. *Space Weather*, 15:1562–1566, December 2017.
- [8] J. T. Hoeksema, J. M. Wilcox, and P. H. Scherrer. Structure of the heliospheric current sheet in the early portion of sunspot cycle 21. *J. Geophys. Res.*, 87:10331–10338, December 1982.
- [9] L. K. Jian, C. T. Russell, J. G. Luhmann, P. J. MacNeice, D. Odstrcil, P. Riley, J. A. Linker, R. M. Skoug, and J. T. Steinberg. Comparison of observations at ace and ulysses with enlil model results: Stream interaction regions during carrington rotations 2016–2018. *Solar Physics*, 273(1):179–203, 2011. ISSN 1573-093X.
- [10] I.T. Jolliffe and D.B. Stephenson. *Forecast Verification: A Practitioner’s Guide in Atmospheric Science*. Wiley, 2003. ISBN 9780471497592. URL <https://books.google.com/books?id=Qm2MjWvUyWC>.
- [11] D. J. Knipp. Advances in Space Weather Ensemble Forecasting. *Space Weather*, 14:52–53, February 2016.
- [12] P. Kohutova, F.-X. Bocquet, E. M. Henley, and M. J. Owens. Improving solar wind persistence forecasts: Removing transient space weather events, and using observations away from the Sun-Earth line. *Space Weather*, 14:802–818, October 2016.
- [13] C. O. Lee, J. G. Luhmann, D. Odstrcil, P. J. MacNeice, I. Pater, P. Riley, and C. N. Arge. The solar wind at 1 au during the declining phase of solar cycle 23: Comparison of 3d numerical model results with observations. *Solar Physics*, 254(1):155–183, 2008. ISSN 1573-093X.
- [14] R. H. Levine, M. D. Altschuler, and J. W. Harvey. Solar sources of the interplanetary magnetic field and solar wind. *J. Geophys. Res.*, 82:1061–1065, March 1977.
- [15] A. Light and P. J. Bartlein. The End of the Rainbow? Color Schemes for Improved Data Graphics. *EOS Transactions*, 85:385–391, October 2004.
- [16] J. A. Linker, Z. Mikić, D. A. Biesecker, R. J. Forsyth, S. E. Gibson, A. J. Lazarus, A. Lecinski, P. Riley, A. Szabo, and B. J. Thompson. Magnetohydrodynamic modeling of the solar corona during Whole Sun Month. *J. Geophys. Res.*, 104:9809–9830, May 1999.
- [17] J. G. Luhmann, Y. Li, C. N. Arge, P. R. Gazis, and R. Ulrich. Solar cycle changes in coronal holes and space weather cycles. *Journal of Geophysical Research (Space Physics)*, 107:1154, August 2002.
- [18] P. MacNeice. Validation of community models: Identifying events in space weather model timelines. *Space Weather*, 7:S06004, June 2009.
- [19] P. MacNeice. Validation of community models: 2. Development of a baseline using the Wang-Sheeley-Arge model. *Space Weather*, 7:S12002, December 2009.
- [20] S. L. McGregor, W. J. Hughes, C. N. Arge, and M. J. Owens. Analysis of the magnetic field discontinuity at the potential field source surface and schatten current sheet interface in the wang?sheeley?arge model. *Journal of Geophysical Research: Space Physics*, 113(A8), 2008. URL <https://agupubs.onlinelibrary.wiley.com/doi/abs/10.1029/2007JA012330>.
- [21] Z. Mikić, J. A. Linker, D. D. Schnack, R. Lionello, and A. Tarditi. Magnetohydrodynamic modeling of the global solar corona. *Physics of Plasmas*, 6:2217–2224, May 1999.
- [22] S. A. Murray. The importance of ensemble techniques for operational space weather forecasting. *ArXiv e-prints*, June 2018.

- [23] L. Nikolic. Modelling the magnetic field of the solar corona with potential-field source-surface and Schatten current sheet models. *Geological Survey of Canada, Open File 8007*, May 2017.
- [24] L. Nikolic, L. Trichtchenko, and D. Boteler. A Numerical Framework for Operational Solar Wind Prediction. *Plasma Fusion Res.*, 9, 2014.
- [25] D. Odstrcil. Modeling 3-D solar wind structure. *Advances in Space Research*, 32:497–506, August 2003.
- [26] M. J. Owens and R. J. Forsyth. The Heliospheric Magnetic Field. *Living Reviews in Solar Physics*, 10(1):5, December 2013. ISSN 2367-3648, 1614-4961.
- [27] M. J. Owens, C. N. Arge, H. E. Spence, and A. Pembroke. An event-based approach to validating solar wind speed predictions: High-speed enhancements in the wang-sheeley-arge model. *Journal of Geophysical Research: Space Physics*, 110(A12):n/a–n/a, 2005. ISSN 2156-2202. A12105.
- [28] M. J. Owens, H. E. Spence, S. McGregor, W. J. Hughes, J. M. Quinn, C. N. Arge, P. Riley, J. Linker, and D. Odstrcil. Metrics for solar wind prediction models: Comparison of empirical, hybrid, and physics-based schemes with 8 years of L1 observations. *Space Weather*, 6:S08001, August 2008.
- [29] M. J. Owens, R. Challen, J. Methven, E. Henley, and D. R. Jackson. A 27 day persistence model of near-earth solar wind conditions: A long lead-time forecast and a benchmark for dynamical models. *Space Weather*, 11(5): 225–236, 2013. ISSN 1542-7390.
- [30] M. J. Owens, P. Riley, and T. S. Horbury. Probabilistic Solar Wind and Geomagnetic Forecasting Using an Analogue Ensemble or “Similar Day” Approach. *Solar Phys.*, 292:69, May 2017.
- [31] V. Pizzo. A three-dimensional model of corotating streams in the solar wind. I - Theoretical foundations. *J. Geophys. Res.*, 83:5563–5572, December 1978.
- [32] J. Pomoell and S. Poedts. EUHFORIA: European heliospheric forecasting information asset. *Journal of Space Weather and Space Climate*, 8(27):A35, June 2018.
- [33] M. A. Reiss, M. Temmer, A. M. Veronig, L. Nikolic, S. Vennerstrom, F. Schoengassner, and S. J. Hofmeister. Verification of high-speed solar wind stream forecasts using operational solar wind models. *Space Weather*, 14(7): 2016SW001390, July 2016. ISSN 1542-7390.
- [34] I. G. Richardson, E. W. Cliver, and H. V. Cane. Sources of geomagnetic activity over the solar cycle: Relative importance of coronal mass ejections, high-speed streams, and slow solar wind. *J. Geophys. Res.*, 105:18, August 2000.
- [35] P. Riley and R. Lionello. Mapping Solar Wind Streams from the Sun to 1 AU: A Comparison of Techniques. *Solar Phys.*, 270:575–592, June 2011.
- [36] P. Riley and J. G. Luhmann. Interplanetary Signatures of Unipolar Streamers and the Origin of the Slow Solar Wind. *Solar Phys.*, 277:355–373, April 2012.
- [37] P. Riley, J. A. Linker, and Z. Mikić. An empirically-driven global MHD model of the solar corona and inner heliosphere. *J. Geophys. Res.*, 106:15889–15902, August 2001.
- [38] P. Riley, R. Lionello, J. A. Linker, Z. Mikic, J. Luhmann, and J. Wijaya. Global MHD Modeling of the Solar Corona and Inner Heliosphere for the Whole Heliosphere Interval. *Solar Phys.*, 274:361–377, December 2011.
- [39] P. Riley, J. A. Linker, and Z. Mikić. On the application of ensemble modeling techniques to improve ambient solar wind models. *Journal of Geophysical Research (Space Physics)*, 118:600–607, February 2013.
- [40] P. Riley, J. A. Linker, and Z. Mikić. Ensemble modeling of the ambient solar wind. *Solar Wind 13*, 1539:259–262, June 2013.
- [41] P. Riley, J. A. Linker, and C. N. Arge. On the role played by magnetic expansion factor in the prediction of solar wind speed. *Space Weather*, 13:154–169, March 2015.
- [42] P. Riley, M. Ben-Nun, J. A. Linker, M. J. Owens, and T. S. Horbury. Forecasting the properties of the solar wind using simple pattern recognition. *Space Weather*, 15:526–540, March 2017.
- [43] S. Robbins, C. J. Henney, and J. W. Harvey. Solar Wind Forecasting with Coronal Holes. *Solar Phys.*, 233: 265–276, February 2006.
- [44] T. Rollett, C. Möstl, A. Isavnin, J. A. Davies, M. Kubicka, U. V. Amerstorfer, and R. A. Harrison. ElEvoHI: A Novel CME Prediction Tool for Heliospheric Imaging Combining an Elliptical Front with Drag-based Model Fitting. *Astrophys. J.*, 824:131, June 2016.
- [45] C. Sanderson and R. Curtin. Armadillo: a template-based C++ library for linear algebra. *The Journal of Open Source Software*, 1:26, June 2016.

- [46] K. H. Schatten. Current sheet magnetic model for the solar corona. *Cosmic Electrodynamics*, 2:232–245, 1971.
- [47] K. H. Schatten, J. M. Wilcox, and N. F. Ness. A model of interplanetary and coronal magnetic fields. *Solar Phys.*, 6:442–455, March 1969.
- [48] C. J. Schrijver et al. Understanding space weather to shield society: A global road map for 2015-2025 commissioned by COSPAR and ILWS. *Advances in Space Research*, 55:2745–2807, June 2015.
- [49] Y. S. Shugay, I. S. Veselovsky, D. B. Seaton, and D. Berghmans. Hierarchical approach to forecasting recurrent solar wind streams. *Solar System Research*, 45:546–556, December 2011.
- [50] O. C. St. Cyr, J. T. Burkepile, A. J. Hundhausen, and A. R. Lecinski. A comparison of ground-based and spacecraft observations of coronal mass ejections from 1980-1989. *J. Geophys. Res.*, 104:12493–12506, June 1999.
- [51] G. Tóth, B. van der Holst, and Z. Huang. Obtaining Potential Field Solutions with Spherical Harmonics and Finite Differences. *Astrophys. J.*, 732:102, May 2011.
- [52] G. Tóth et al. Space Weather Modeling Framework: A new tool for the space science community. *Journal of Geophysical Research (Space Physics)*, 110:A12226, December 2005.
- [53] B. Vršnak, M. Temmer, and A. M. Veronig. Coronal Holes and Solar Wind High-Speed Streams: I. Forecasting the Solar Wind Parameters. *Solar Phys.*, 240:315–330, February 2007.
- [54] Y.-M. Wang and N. R. Sheeley, Jr. Solar wind speed and coronal flux-tube expansion. *Astrophys. J.*, 355:726–732, June 1990.
- [55] Y.-M. Wang and N. R. Sheeley, Jr. Solar Implications of ULYSSES Interplanetary Field Measurements. *Astrophys. J. Lett.*, 447:L143, July 1995.